Article

Vectorial holograms with a dielectric metasurface: ultimate polarization pattern generation

Ehsan Arbabi, Seyedeh Mahsa Kamali, Amir Arbabi, and Andrei Faraon

ACS Photonics, **Just Accepted Manuscript** • DOI: 10.1021/acsphotonics.9b00678 • Publication Date (Web): 18 Sep 2019

Vectorial holograms with a dielectric metasurface: ultimate polarization pattern generation

Ehsan Arbabi,[†,‡] Seyedeh Mahsa Kamali,[†,‡] Amir Arbabi,[¶] and Andrei Faraon[*,†,‡]

†*T. J. Watson Laboratory of Applied Physics and Kavli Nanoscience Institute, California Institute of Technology, 1200 E. California Blvd., Pasadena, CA 91125, USA*

‡*Department of Electrical Engineering, California Institute of Technology, 1200 E. California Blvd., Pasadena, CA 91125, USA*

¶*Department of Electrical and Computer Engineering, University of Massachusetts Amherst, 151 Holdsworth Way, Amherst, MA 01003, USA*

E-mail: faraon@caltech.edu

Abstract

Controlling the polarization of light has been of interest for various applications in laser materials processing, display systems, and spectroscopy among others. Despite great advancements, the level of control over the polarization of light using naturally birefringent materials and liquid crystals is still limited. In recent years, dielectric metasurfaces have enabled an unprecedented control over the polarization and phase of light. Here, we demonstrate vectorial holograms with almost arbitrary polarization patterns using structurally birefringent dielectric metasurfaces. Using a modified Gerchberg-Saxton algorithm and converting the red-green-blue data in arbitrary color images to Stokes parameters, we show that the demonstrated metasurfaces can store and project color image data in the polarization state of a monochromatic

hologram. In addition to holograms with enhanced security and data storage capacity, we believe that the developed concepts and methods will spur new applications in advanced structured illumination techniques, and more generally, whenever a complex polarization pattern is required.

Keywords

Optical metasurface, flat optics, polarization optics, polarization hologram, vectorial hologram

Polarization is an important property of light that can be used for storing and transferring information. Its control has been of great interest for various applications in display systems,[1,2] particle trapping,[3,4] laser materials processing,[5,6] and polarized Raman spectroscopy.[7,8] Polarization has conventionally been manipulated using naturally birefringent materials. Polarization holograms are in general two or three dimensional holograms with a spatially varying degree or direction of birefringence,[9–12] encoding phase, polarization, and/or amplitude data. Computer generated polarization holograms have mostly been utilized to store phase information using the geometric phase and perform as polarization dependent gratings, lenses, and holograms.[10,13–15] While polarization holograms can in principle be used to control the phase and amplitude,[16] or phase and polarization simultaneously,[17] limited phase control levels, complex fabrication, and large pixel sizes significantly limit their applicability for these purposes.

Computer generated polarization holograms implemented using structural birefringence and fabricated using conventional micro-fabrication techniques[18–23] overcome some of the limitations of conventional polarization holograms as they achieve higher resolutions, enable more precise control of phase and birefringence, and are easier to fabricate. Nevertheless, the level of control over polarization and phase is still very limited in these structures. Metasurfaces, two-dimensional rational arrangements of scatterers,[24–31] have in recent years enabled full and simultaneous control of polarization and phase on a subwavelength lattice and with high efficiency.[32] Most demonstrations so far have either focused on solely controlling the polarization[33–35] or independent control

of phase for two orthogonal polarizations.[36–40] Another important application of the concept and platform is the simultaneous control of polarization and phase.[32] Although this ability has been partially utilized to demonstrate metasurfaces that shape the beam and work as half-wave plates simultaneously,[41,42] its full potential has not been explored yet.

Here, we employ the previously developed simultaneous polarization and phase control capability of high-contrast dielectric measurfaces[32] to demonstrate a new category of polarization holograms, where the electric field vector is controlled independently on each point of the mask. The holograms project vectorial images in which the data is stored in the state of polarization. We propose and employ a modified Gerchberg-Saxton (GS) algorithm that enables the design of these vectorial holograms. Given the existence of three independent degrees of freedom in the polarization of light for fully polarized beams, we experimentally show that these vectorial holograms can store and project the data in arbitrary red-green-blue (RGB) full-color images. It is worth noting that diatomic plasmonic as well as high-contrast dielectric metasurfaces were recently used to demonstrate vectorial holograms.[43,44] However, the vectorial holograms demonstrated in[43,44] are basically spatial superpositions of multiple holograms that have specific output polarizations (e.g., the metasurface consists of a few spatially multiplexed holograms projecting images with different polarization states). In addition to a lower efficiency, there are several problems with a spatial multiplexing scheme for such polarization holograms. Some of these issues are a significantly lower degree of control over the polarization state distribution of the hologram, much lower complexity in the polarization state of the projected image, and lower hologram quality due to an effectively smaller aperture for each sub-part of the hologram. Moreover, in areas where the different subparts of the hologram overlap, the overall polarization state is not controllable (and in general ends up having a random state of polarization) because the phase distribution over the hologram area is not controlled. In contrast, the metasurface holograms demonstrated in this manuscript act as whole to create polarization patterns of arbitrary complexity as evidenced by the encoded RGB images.

Figure **1** shows a schematic of a metasurface and the color-encoded polarization hologram gen-

erated. The metasurface is illuminated by a beam with known wavelength and polarization state. The dielectric metasurface, made up of high refractive index nano-posts, enables simultaneous and independent control of the output light's phase and polarization.[32] Since each nano-post operates almost independently, this full control can be implemented on a subwavelength lattice. This allows for an unprecedented control of the vectorial electric field transmitted through the metasurface. As we show in the following, this control can be utilized to encode the data of a color image into the polarization state of light projected by the metasurface.

Polarization of light can be fully characterized using the Stokes parameters S_0, S_1, S_2, and S_3, usually defined as $S_0 = I$, $S_1 = I_{\mathrm{x}} - I_{\mathrm{y}}$, $S_2 = I_{45} - I_{-45}$, and $S_3 = I_{\mathrm{R}} - I_{\mathrm{L}}$. Here, I denotes the total light intensity, I_{x} and I_{y} are the partial intensities of light linearly polarized along the x and y axes, I_{45} and I_{-45} are the intensities in the linear bases along +45° and -45° axes, and I_{R} and I_{L} denote the right hand and left hand circular intensities, respectively. For fully polarized light, the four parameters are related through the relation $S_0 = \sqrt{{S_1}^2 + {S_2}^2 + {S_3}^2}$. This, reduces the number of independent parameters to three, which in a different representation correspond to the amplitude of the electric field along the x and y axes and their phase difference. We would like to note here that the three Stokes parameters S_1, S_2, and S_3 can be used as completely independent parameters to represent any three-dimensional space, as long as the fourth one S_0 (i.e., the total light intensity) is left to vary freely.

As shown in Figs. **2a** and **2b**, the red, green, and blue components of a color image can be mapped to the Stokes parameters S_1, S_2, and S_3 through a simple linear transformation that maps the color ranges to the [-1,1] interval. Figure **2c** shows the distribution of the pixels of the image shown in Fig. **2a** on the Poincare sphere. This shows that the points cover a very large portion of possible polarization states, denoting the capability of the method to generate images with arbitrarily complex polarization distributions. Finally, for the actual hologram design process it is more useful to use the electric field representation of polarization, which is possible as the light is fully polarized. Figure **2d** shows the amplitudes of the electric field along the x and y axes, $|E_x|$ and $|E_y|$, and their phase difference, $\phi = \angle E_y - \angle E_x$, which are calculated form the Stokes parameters

plotted in Fig. **2b**.

To design the metasurface, we developed and used a modified GS algorithm. As shown in Fig. **3**, the field right before the metasurface has an amplitude of one and is polarized along the x axis. The field right after the metasurface can have any arbitrary polarization and phase distributions, however, it has a unity amplitude, i.e., $\sqrt{|{E_x}^m|^2 + |{E_y}^m|^2} = 1$. On the hologram plane in the far field, polarization and amplitude distributions ($|{E_x}^h|$, $|{E_y}^h|$, and ϕ) are set, while the relative phases between different points, $\angle {E_x}^h$, are available degrees of freedom. We start the design process by assigning a uniform phase to the field in the hologram plane, and setting the initial hologram fields as follows:

$$\begin{aligned} {E_x}^h(1) &= |{E_x}^h| \\ {E_y}^h(1) &= |{E_y}^h| \mathrm{e}^{j\phi} \end{aligned} . \tag{1}$$

At each subsequent step, the metasurface field is calculated through the following Fourier transform relations:

$$\begin{aligned} {E_x}^m(i) &= \frac{\mathcal{F}[{E_x}^h(i)]}{I(i)} \\ {E_y}^m(i) &= \frac{\mathcal{F}[{E_y}^h(i)]}{I(i)} \\ I(i) &= \sqrt{\mathcal{F}[{E_x}^h(i)]^2 + \mathcal{F}[{E_y}^h(i)]^2} \end{aligned} , \tag{2}$$

where i is the iteration step, $\mathcal{F}[\cdot]$ represents the Fourier transform operator, and $I(i)$ is the total intensity used to normalize the field as it should have a unity amplitude. The hologram fields in the next iterations should satisfy $\phi = \angle E_y - \angle E_x$. Therefore, in each step we can only set the phase of one polarization from the GS algorithm, and the phase of the other polarization should be calculated using the known phase difference, ϕ. To make the process symmetric for the two

polarizations, we alternate between them in each pair of iterations, i.e.,

$$\begin{cases} i \text{ is even}: \begin{cases} {E_x}^h(i) = |{E_x}^h|\exp(j\angle\mathcal{F}^{-1}[{E_x}^m(i-1)]) \\ {E_y}^h(i) = |{E_y}^h|\exp(j\angle\mathcal{F}^{-1}[{E_x}^m(i-1)]+j\phi) \end{cases} \\ i \text{ is odd}: \begin{cases} {E_x}^h(i) = |{E_x}^h|\exp(j\angle\mathcal{F}^{-1}[{E_y}^m(i-1)]-j\phi) \\ {E_y}^h(i) = |{E_y}^h|\exp(j\angle\mathcal{F}^{-1}[{E_y}^m(i-1)]) \end{cases} \end{cases} . \quad (3)$$

In the examples used in this work, the modified algorithm converged to the final designs in less than twenty iterations. It is worth noting here that as the hologram operates primarily as a phase hologram, it has a relatively low sensitivity to amplitude variations. Therefore, if the metasurface transmittance (albeit above 90% on average) is lower in some areas than others, it does not significantly deteriorate the hologram performance.

After determining the required field distributions on the metasurface, we need to design a metasurface structure that can generate these field distributions with high efficiency. We used the high-contrast dielectric metasurface structure that enables full control of output polarization and phase.[32,38] As shown in Figs. **4a**, **b**, and **d**, the metasurface is based on high-index cuboid nano-posts with different dimensions along the x and y axes, a and b, respectively. For proper choices of the nano-posts height and distance, the transmission phases can be controlled independently from 0 to 2π, while keeping the transmission amplitude close to 1. For the operation wavelength of 850 nm, we used amorphous silicon (α-Si) nano-posts that are 682-nm tall and located on a square lattice with a 420-nm long lattice constant. Figure **4c** shows the nano-post side lengths, a and b, versus the transmission phases for x- and y-polarized light.

As demonstrated in,[32,38] the metasurface structure of Fig. **4** can control the phase and polarization of output light independently on a subwavelength lattice. Specifically, when the transmittance of the metasurface is close to unity, the transmission of the nano-post shown in **4d** can be modeled

as $\mathbf{E}^{\text{out}} = \mathbf{T}\mathbf{E}^{\text{in}}$, where the Jones matrix $\mathbf{T}$ is given by:[32,38]

$$\mathbf{T} = \begin{bmatrix} T_{xx} & T_{xy} \\ T_{yx} & T_{yy} \end{bmatrix} = \mathbf{R}(\theta) \begin{bmatrix} \mathrm{e}^{i\phi_{x'}} & 0 \\ 0 & \mathrm{e}^{i\phi_{y'}} \end{bmatrix} \mathbf{R}(-\theta), \tag{4}$$

where $\mathbf{R}(\theta)$ denotes the rotation matrix by an angle θ in the counter-clockwise direction, and $\phi_{x'}$ and $\phi_{y'}$, show the transmission phases along the two axes of the nano-post. Using the unitarity and symmetry of the Jones matrix, we can rewrite equations in terms of the unknown Jones matrix elements:[32,38]

$$\begin{bmatrix} E_x^{\text{out}*} & E_y^{\text{out}*} \\ E_x^{\text{in}} & E_y^{\text{in}} \end{bmatrix} \begin{bmatrix} T_{xx} \\ T_{yx} \end{bmatrix} = \begin{bmatrix} E_x^{\text{in}*} \\ E_x^{\text{out}} \end{bmatrix}. \tag{5}$$

Therefore, once the input and output electric field vectors are known at each point on the meta-surface, the corresponding Jones matrix can be calculated from Eq. 5. Then, the required rotation angle θ and phase pairs, $\phi_{x'}$ and $\phi_{y'}$, can be calculated using Eq. 4. The data in Fig. **4c** can then be used to find the nano-post that provides the required phases.

Finally, in order to experimentally demonstrate the capability of the proposed method and structure to generate polarization holograms, we designed and fabricated different polarization holograms that project the data in a few color images. The process used to fabricate the devices has been previously discussed in several publications.[32,38,45] In short, a layer of α-Si was deposited on a fused silica substrate. The metasurface pattern was defined using electron-beam lithography and reversed through evaporation and lift-off of an aluminum oxide layer. This layer was used as a hard mask in dry etching of α-Si and was removed after the etch step. And optical and an scanning electron microscope image of the fabricated device are shown in Figs. **4e** and **4f**, respectively.

To measure the hologram, we used a custom-built microscope that imaged the back-focal plane of an objective lens on an image sensor using a 4-f system (Fig. **5a**). We used a linear polarizer to set the input polarization along the x axis. In addition, a polarization analyzer composed of a quarter waveplate and a linear polarizer was used inside the 4-f system to measure the hologram Stokes parameters. The measured Stokes parameters are then converted back to RGB data and

combined to form the measured holograms.

The original, simulated, and measured color images are shown in Figs. **5b** and **5c** for two images. Both holograms are about 30 degrees in height, corresponding to a diagonal numerical aperture (NA) of 0.36 for the hologram in Fig. **5b**. The design process was exactly similar for two example images, and started by calculating the Stokes parameters from the RGB data, as shown in Figs. **2a** and **b**, which correspond to the hologram of Fig. **5b**. The initial electric field distribution of the hologram was then calculated from the Stokes parameters (Fig. **2d**), and the modified GS algorithm was used to calculate the required metasurface electric field distributions as well as the simulated polarization holograms (the middle images shown in Figs. **5b** and **5c**). Assuming an input electric field polarized along the x axis, the corresponding nano-posts were found through the process explained in the previous paragraph.

It is worth noting that different linear transformations might be used for mapping specific colors to specific intensities. Here, using 8-bit color images where the RGB values change from 0 to 255 for each color, we simply used the linear relation $S_i = (X - 128)/128$, where i can be 1, 2, or 3 and X denotes R, G, or B, respectively. However, one might want to have a different color mapping, for instance convert black to an intensity of zero. This might simply be possible either through using only half of the possible existing polarization states, i.e., by setting $S_i \geq 0$, or using a more complicated mapping.

An alternative design method is possible where all the nano-posts have the same rotation axis (i.e., all nano-posts have $\theta = \theta_0$). In that design, there is no conversion between the two linear polarizations along the two axes of the nano-posts, which we can call x and y without loss of generality. As a result, the input and output x-polarized (as well as y-polarized) powers should be equal, which means that the input polarization should be chosen based on the axes directions and the desired hologram. In addition, the normalization step in the hologram design algorithm (i.e., Eq. 3) would be slightly different for this method. We simulated the same polarization holograms using this alternative method, and did not observe any significant difference in their performance.

With proper choice of materials and scaling the designs, it is straightforward to generalize the

concept and the devices to other wavelengths. For instance, titanium dioxide metasurfaces have been shown to achieve similar control abilities over the phase and polarization of light[36,46] in the visible wavelengths. It is worth noting, however, that these devices typically have lower efficiency mainly due to lower index contrast and higher sensitivity to fabrication errors.

The new capabilities of dielectric metasurfaces in simultaneous control of phase and polarization allow for implementation of new categories of devices with no conventional counterparts. Here, we demonstrated vectorial holograms that generate polarization patterns of almost arbitrary complexity, designed using a modified GS algorithm. The devices operate in the near infrared and are based on an α-Si birefringent metasurface. The same method and structure can readily be used in other wavelength ranges using various materials.[46,47] While the demonstrated concepts and methods can be used to make holograms with enhanced security and added data storage capabilities, we expect that they spur more important applications in advanced structured illumination schemes or vectorial beam generation.

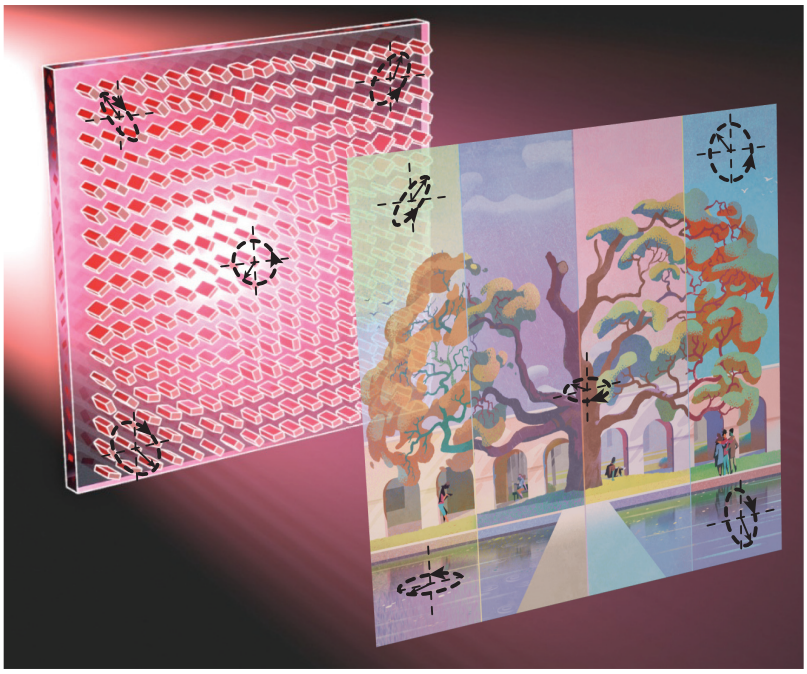

Figure 1: **Schematic illustration of a metasurface polarization hologram, projecting a polarization pattern encoding an RGB image.** The metasurface is illuminated with a beam of known wavelength and polarization. Each dielectric nano-post is designed to control the polarization and phase of the output light at its location. The artistic illustration is used with permission from Caltech and the artist Rustam Hasanov.

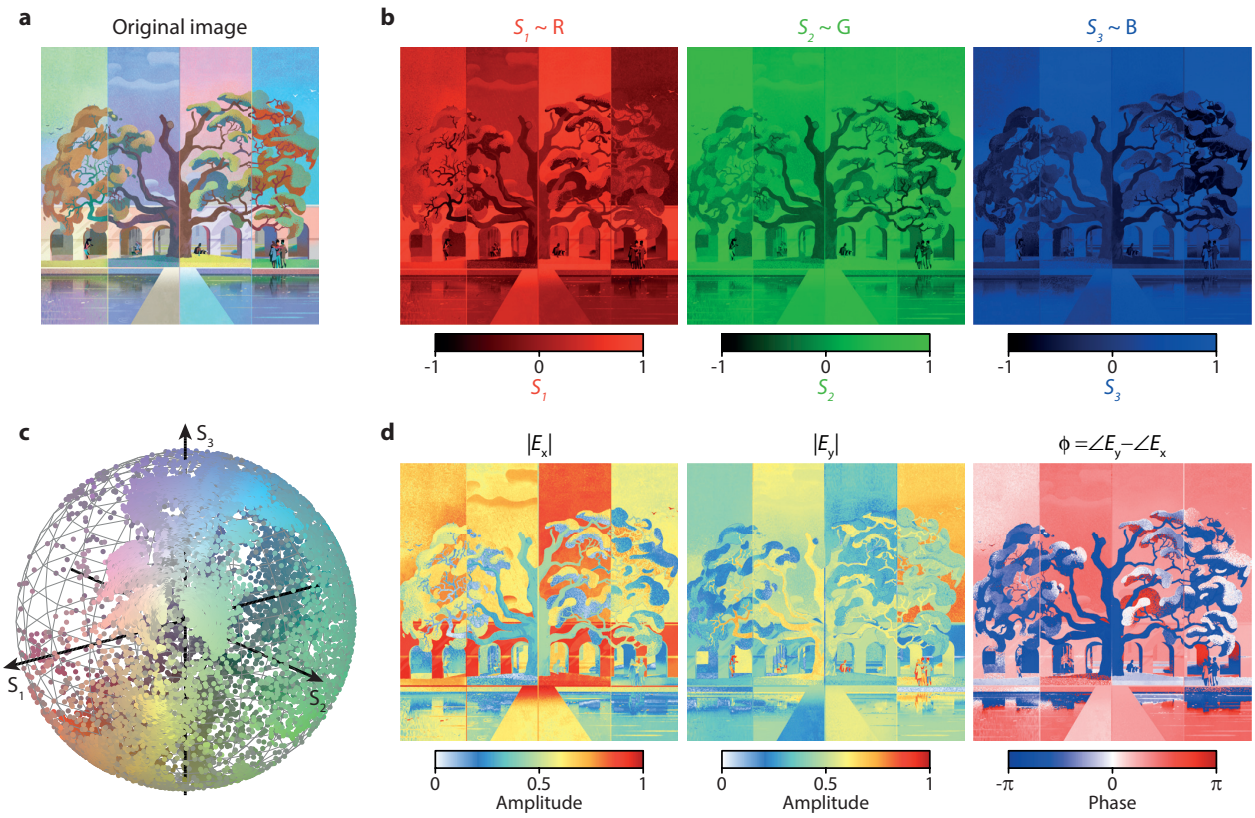

Figure 2: **Mapping an RGB image data to polarization.** **(a)** The original RGB image. **(b)** The red, green, and blue components of the image in **a**, corresponding to the Stokes parameters characterizing the polarization pattern. **(c)** The Poincare sphere representation of the polarization pattern corresponding to the image in **a**. The position of each point and its color demonstrate the polarization and intensity of light at one point in the image. For the data to be more clear, only about two percent of the original image pixels are shown. **(d)** The electric field amplitudes along the *x* and *y* axes and their phase difference, calculated from the Stokes parameters in **b**. This data is directly used in the metasurface hologram design algorithm through a modified GS algorithm. The artistic illustration in panels **a**, **b**, and **d** is used with permission from Caltech and the artist Rustam Hasanov.

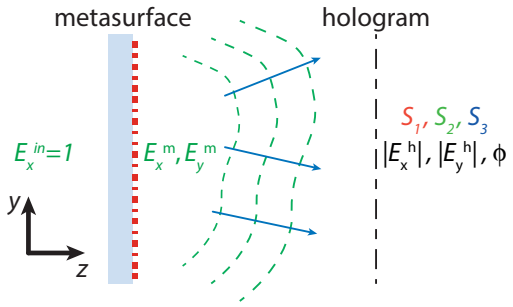

Figure 3: Schematic of a metasurface projecting a desired polarization pattern. The projected polarization pattern is characterized by the Stokes parameters S_1, S_2, and S_3, and the required electric field vector on the metasurface, with components $E_x{}^m$ and $E_y{}^m$, is calculated using the modified GS algorithm.

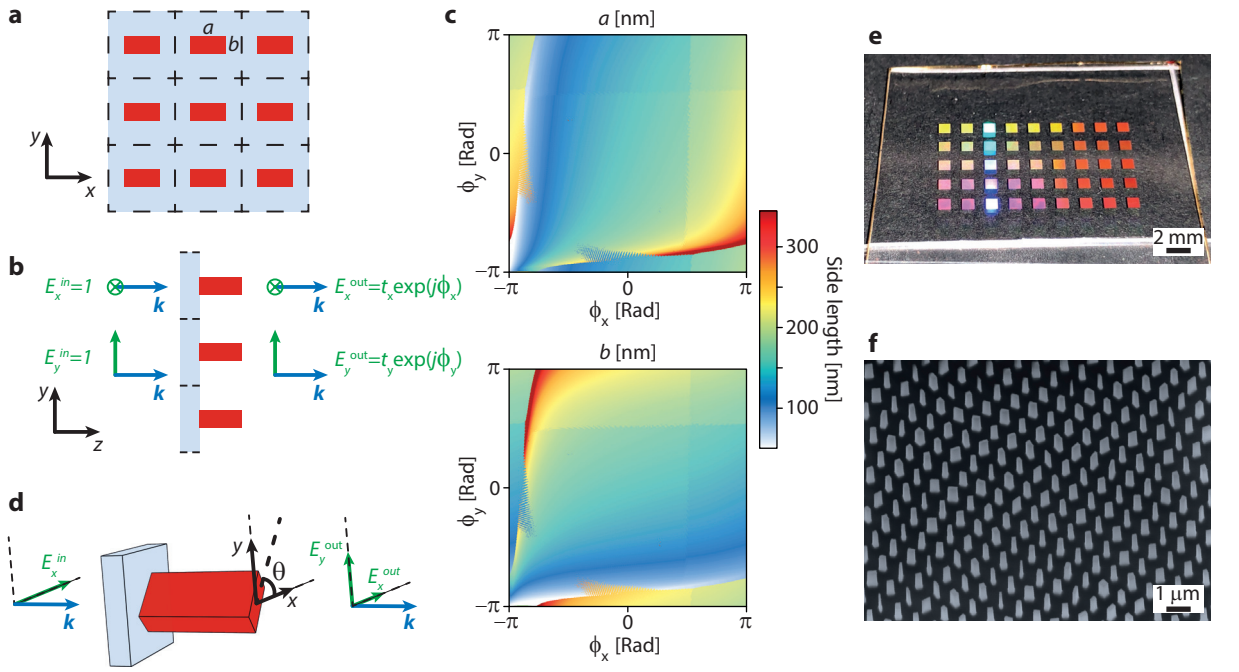

Figure 4: **Metasurface structure and design graphs.** **(a)** Schematics of a uniform lattice of dielectric nano-posts showing the post dimensions. **(b)** Side-view of the uniform array of nano-posts, showing the transmission parameters along the x and y axes. With a proper choice of the material, lattice constant, and post height, ϕ_x and ϕ_y can be fully and independently controlled to cover the whole 0–2π range. **(c)** Chosen values of a and b for achieving ϕ_x and ϕ_y. **(d)** Simultaneous control of the output polarization and phase by rotating the nano-post with correspondingly chosen dimensions. The nano-post can generate an output field with any arbitrary polarization and phase from any given input polarization. **(e)** An optical image of the fabricated polarization holograms. **(f)** Scanning electron micrograph of a part of the fabricated hologram.

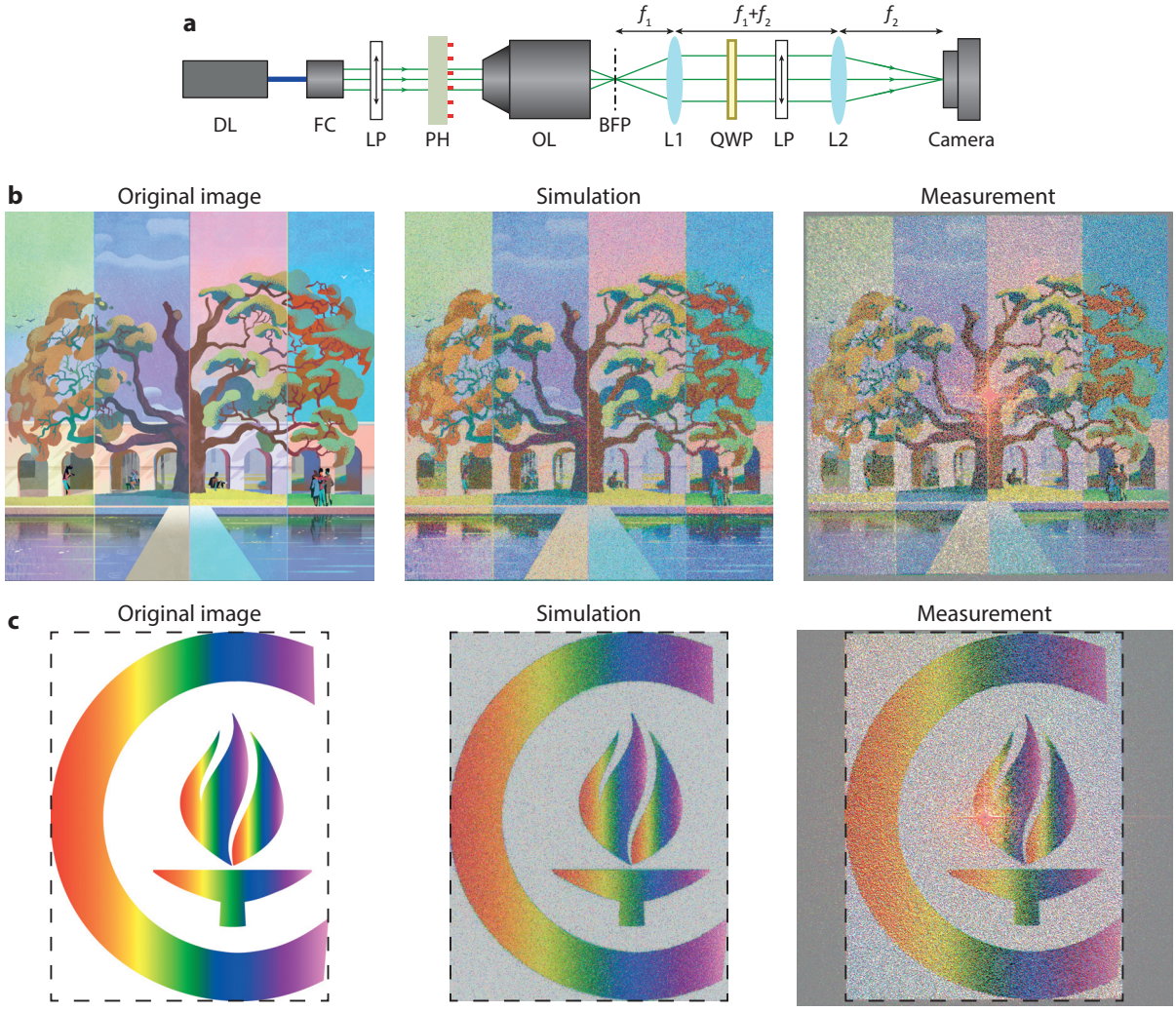

Figure 5: **Simulation and measurement results.** **(a)** Schematic of the optical setup used to characterize the polarization holograms. A 4-f system (L_1 and L_2) is used to image the back focal plane of the objective on the camera. DL: Diode laser; FC: Fiber collimator; LP: Linear polarizer; PH: Polarization hologram; OL: Objective lens; BFP: Back focal plane; L1 and L2: Lenses; QWP: Quarter waveplate. **(b, c)** The original target image along with simulated and measured polarization holograms converted to false-color images. Both holograms are about 30-degrees tall, corresponding to a diagonal NA of 0.36 for the holograms in panel **b**. The artistic illustration in panel **b** is used with permission from Caltech and the artist Rustam Hasanov. The Caltech icon in panel **c** is used with permission from Caltech.

Methods

Simulation. The rigorous coupled wave analysis technique[48] was used to calculate the transmission amplitude and phase of the rectangular nano-posts. The refractive indices of α-Si and fused silica were assumed to be 3.6 and 1.45 at the operation wavelength of 850 nm. The sizes of nano-posts that provide a specific phase pair plotted in Fig. **4c** are found through minimizing the total complex error $|t_x - \exp(i\phi_x)|^2 + |t_y - \exp(i\phi_y)|^2$. The holograms are designed using Eqs. 1-3, where the fast Fourier transform technique is used to calculate the discrete Fourier transforms. The algorithm converged to the final designs in less than 20 iterations in all cases.

Sample fabrication. The α-Si layer was deposited on the fused silica substrate using the plasma enhanced chemical vapor deposition to a final thickness of 682 nm. The metasurface pattern was generated using an EBPG5200 electron beam lithography machine in a positive electron resist (ZPE-520A). An electron beam evaporated aluminum oxide layer was used to reverse the generated pattern with a lift-off process, and was then used as a hard mask for dry etching the α-Si layer. The aluminum oxide layer was then dissolved in a mixture of hydrogen peroxide and ammonium hydroxide.

Measurement procedure. The measurement setup is shown in Fig. **5a**. The metasurface was illuminated by an x-polarized collimated beam from an $\sim$850-nm laser diode. An objective lens (LMPlanFl 20$\times$, NA=0.4; Olympus) was used to form a Fourier transform of the metasurface hologram in its back focal plane. A 4-f system (LB1471-B, f=50 mm and LB1437-B, f=150 mm; Thorlabs Inc.) was then used to image the back focal plane onto a charge-coupled device image sensor (CoolSNAP K4; Photometrics). A polarization state analyzer formed from a quarter wave-plate (AQWP10M-980; Thorlabs Inc.) and a linear polarizer (LPVIS100-MP2; Thorlabs Inc.), placed inside the 4-f system, was used to measure the Stokes parameters of the holograms. The measured Stokes parameters were numerically combined and converted to color data to form the final false-color holograms.

The authors declare no competing financial interest.

Acknowledgement

This work was supported by the DARPA EXTREME program. We gratefully acknowledge critical support and infrastructure provided for this work by the Kavli Nanoscience Institute at Caltech.

References

(1) Zhu, X.; Ge, Z.; Wu, T. X.; Wu, S.-T. Transflective Liquid Crystal Displays. *J. Display Technol.* **2005**, *1*, 15.

(2) Yang, D.-K. *Fundamentals of liquid crystal devices*; John Wiley & Sons, 2014.

(3) Zhan, Q. Trapping metallic Rayleigh particles with radial polarization. *Opt. Express* **2004**, *12*, 3377–3382.

(4) Kozawa, Y.; Sato, S. Optical trapping of micrometer-sized dielectric particles by cylindrical vector beams. *Opt. Express* **2010**, *18*, 10828–10833.

(5) Meier, M.; Romano, V.; Feurer, T. Material processing with pulsed radially and azimuthally polarized laser radiation. *Appl. Phys. A* **2007**, *86*, 329–334.

(6) Weber, R.; Michalowski, A.; Abdou-Ahmed, M.; Onuseit, V.; Rominger, V.; Kraus, M.; Graf, T. Effects of Radial and Tangential Polarization in Laser Material Processing. *Physics Procedia* **2011**, *12*, 21–30.

(7) Duesberg, G. S.; Loa, I.; Burghard, M.; Syassen, K.; Roth, S. Polarized Raman Spectroscopy on Isolated Single-Wall Carbon Nanotubes. *Phys. Rev. Lett.* **2000**, *85*, 5436–5439.

(8) Benevides, J. M.; Overman, S. A.; Thomas Jr, G. J. Raman, polarized Raman and ultraviolet resonance Raman spectroscopy of nucleic acids and their complexes. *J. Raman Spectrosc.* **2005**, *36*, 279–299.

(9) Bryngdahl, O. Polarizing Holography. *J. Opt. Soc. Am.* **1967**, *57*, 545–546.

(10) Nakajima, M.; Komatsu, H.; Mitsuhashi, Y.; Morikawa, T. Computer generated polarization holograms: phase recording by polarization effect in photodichroic materials. *Appl. Opt.* **1976**, *15*, 1030–1033.

(11) Nikolova, L.; Todorov, T. Diffraction Efficiency and Selectivity of Polarization Holographic Recording. *Optica Acta* **1984**, *31*, 579–588.

(12) Todorov, T.; Nikolova, L.; Tomova, N. Polarization holography. 2: Polarization holographic gratings in photoanisotropic materials with and without intrinsic birefringence. *Appl. Opt.* **1984**, *23*, 4588–4591.

(13) Oh, C.; Escuti, M. J. Achromatic diffraction from polarization gratings with high efficiency. *Opt. Lett.* **2008**, *33*, 2287–2289.

(14) Kim, J.; Li, Y.; Miskiewicz, M. N.; Oh, C.; Kudenov, M. W.; Escuti, M. J. Fabrication of ideal geometric-phase holograms with arbitrary wavefronts. *Optica* **2015**, *2*, 958–964.

(15) Jamali, A.; Bryant, D.; Zhang, Y.; Grunnet-Jepsen, A.; Bhowmik, A.; Bos, P. J. Design of a large aperture tunable refractive Fresnel liquid crystal lens. *Appl. Opt.* **2018**, *57*, B10–B19.

(16) Fratz, M.; Fischer, P.; Giel, D. M. Full phase and amplitude control in computer-generated holography. *Optics Letters* **2009**, *34*, 3659–3661.

(17) Fratz, M.; Giel, D. M.; Fischer, P. Digital polarization holograms with defined magnitude and orientation of each pixel's birefringence. *Opt. Lett.* **2009**, *34*, 1270–1272.

(18) Lalanne, P.; Hazart, J.; Chavel, P.; Cambril, E.; Launois, H. A transmission polarizing beam splitter grating. *J. Opt. A Pure Appl. Opt.* **1999**, *1*, 215.

(19) Bomzon, Z.; Kleiner, V.; Hasman, E. Pancharatnam-Berry phase in space-variant polarization-state manipulations with subwavelength gratings. *Opt. Lett.* **2001**, *26*, 1424–1426.

(20) Biener, G.; Niv, A.; Kleiner, V.; Hasman, E. Formation of helical beams by use of Pancharatnam-Berry phase optical elements. *Opt. Lett.* **2002**, *27*, 1875–1877.

(21) Yu, W.; Konishi, T.; Hamamoto, T.; Toyota, H.; Yotsuya, T.; Ichioka, Y. Polarization-multiplexed diffractive optical elements fabricated by subwavelength structures. *Appl. Opt.* **2002**, *41*, 96–100.

(22) Levy, U.; Tsai, C.-H.; Pang, L.; Fainman, Y. Engineering space-variant inhomogeneous media for polarization control. *Opt. Lett.* **2004**, *29*, 1718–1720.

(23) Lin, D.; Fan, P.; Hasman, E.; Brongersma, M. L. Dielectric gradient metasurface optical elements. *Science* **2014**, *345*, 298–302.

(24) Kamali, S. M.; Arbabi, E.; Arbabi, A.; Faraon, A. A review of dielectric optical metasurfaces for wavefront control. *Nanophotonics* **2018**, *7*, 1041–1068.

(25) Kim, I.; Yoon, G.; Jang, J.; Genevet, P.; Nam, K. T.; Rho, J. Outfitting Next Generation Displays with Optical Metasurfaces. *ACS Photonics* **2018**, *5*, 3876–3895.

(26) Lalanne, P.; Chavel, P. Metalenses at visible wavelengths: past, present, perspectives. *Laser Photon. Rev.* **2017**, *11*, 1600295.

(27) Su, V.-C.; Chu, C. H.; Sun, G.; Tsai, D. P. Advances in optical metasurfaces: fabrication and applications [Invited]. *Opt. Express* **2018**, *26*, 13148–13182.

(28) He, Q.; Sun, S.; Xiao, S.; Zhou, L. High-Efficiency Metasurfaces: Principles, Realizations, and Applications. *Adv. Opt. Mater.* **2018**, *6*, 1800415.

(29) Kamali, S. M.; Arbabi, A.; Arbabi, E.; Horie, Y.; Faraon, A. Decoupling optical function and geometrical form using conformal flexible dielectric metasurfaces. *Nat. Commun.* **2016**, *7*, 11618.

(30) Qiao, P.; Yang, W.; Chang-Hasnain, C. J. Recent advances in high-contrast metastructures, metasurfaces, and photonic crystals. *Adv. Opt. Photonics* **2018**, *10*, 180–245.

(31) Colburn, S.; Zhan, A.; Majumdar, A. Metasurface optics for full-color computational imaging. *Sci. Adv.* **2018**, *4*, eaar2114.

(32) Arbabi, A.; Horie, Y.; Bagheri, M.; Faraon, A. Dielectric metasurfaces for complete control of phase and polarization with subwavelength spatial resolution and high transmission. *Nat. Nanotechnol.* **2015**, *10*, 937–943.

(33) Backlund, M. P.; Arbabi, A.; Petrov, P. N.; Arbabi, E.; Saurabh, S.; Faraon, A.; Moerner, W. E. Removing orientation-induced localization biases in single-molecule microscopy using a broadband metasurface mask. *Nat. Photon.* **2016**, *10*, 459–462.

(34) Kruk, S.; Hopkins, B.; Kravchenko, I. I.; Miroshnichenko, A.; Neshev, D. N.; Kivshar, Y. S. Invited Article: Broadband highly efficient dielectric metadevices for polarization control. *APL Photonics* **2016**, *1*, 030801.

(35) Zang, X.; Dong, F.; Yue, F.; Zhang, C.; Xu, L.; Song, Z.; Chen, M.; Chen, P.-Y.; Buller, G. S.; Zhu, Y. e. a. Polarization Encoded Color Image Embedded in a Dielectric Metasurface. *Adv. Mater.* **2018**, *30*, 1707499.

(36) Balthasar Mueller, J. .; Rubin, N. A.; Devlin, R. C.; Groever, B.; Capasso, F. Metasurface Polarization Optics: Independent Phase Control of Arbitrary Orthogonal States of Polarization. *Phys. Rev. Lett.* **2017**, *118*, 113901.

(37) Emani, N. K.; Khaidarov, E.; Paniagua-Dominguez, R.; Fu, Y. H.; Valuckas, V.; Lu, S.; Zhang, X.; Tan, S. T.; Demir, H. V.; Kuznetsov, A. I. High-efficiency and low-loss gallium nitride dielectric metasurfaces for nanophotonics at visible wavelengths. *Appl. Phys. Lett.* **2017**, *111*, 221101.

(38) Arbabi, E.; Kamali, S. M.; Arbabi, A.; Faraon, A. Full-Stokes Imaging Polarimetry Using Dielectric Metasurfaces. *ACS Photonics* **2018**, *5*, 3132–3140.

(39) Kruk, S.; Ferreira, F.; Mac Suibhne, N.; Tsekrekos, C.; Kravchenko, I.; Ellis, A.; Neshev, D.; Turitsyn, S.; Kivshar, Y. Transparent Dielectric Metasurfaces for Spatial Mode Multiplexing. *Laser Photon. Rev.* **2018**, *12*, 1800031.

(40) Arbabi, E.; Li, J.; Hutchins, R. J.; Kamali, S. M.; Arbabi, A.; Horie, Y.; Van Dorpe, P.; Gradinaru, V.; Wagenaar, D. A.; Faraon, A. Two-Photon Microscopy with a Double-Wavelength Metasurface Objective Lens. *Nano Lett.* **2018**, *18*, 4943–4948.

(41) Yang, Y.; Wang, W.; Moitra, P.; Kravchenko, I. I.; Briggs, D. P.; Valentine, J. Dielectric Meta-Reflectarray for Broadband Linear Polarization Conversion and Optical Vortex Generation. *Nano Lett.* **2014**, *14*, 1394–1399.

(42) Kwon, H.; Arbabi, E.; Kamali, S. M.; Faraji-Dana, M.; Faraon, A. Computational complex optical field imaging using a designed metasurface diffuser. *Optica* **2018**, *5*, 924–931.

(43) Deng, Z.-L.; Deng, J.; Zhuang, X.; Wang, S.; Li, K.; Wang, Y.; Chi, Y.; Ye, X.; Xu, J.; Wang, G. P. e. a. Diatomic Metasurface for Vectorial Holography. *Nano Lett.* **2018**, *18*, 2885–2892.

(44) Zhao, R.; Sain, B.; Wei, Q.; Tang, C.; Li, X.; Weiss, T.; Huang, L.; Wang, Y.; Zentgraf, T. Multichannel vectorial holographic display and encryption. *Light Sci. Appl.* **2018**, *7*, 95.

(45) Arbabi, A.; Horie, Y.; Ball, A. J.; Bagheri, M.; Faraon, A. Subwavelength-thick lenses with high numerical apertures and large efficiency based on high-contrast transmitarrays. *Nat. Commun.* **2015**, *6*, 7069.

(46) Rubin, N. A.; Zaidi, A.; Juhl, M.; Li, R. P.; Mueller, J. P. B.; Devlin, R. C.; Lesson, K.; Capasso, F. Polarization state generation and measurement with a single metasurface. *Optics Express* **2018**, *26*, 21455–21478.

(47) Arbabi, E.; Arbabi, A.; Kamali, S. M.; Horie, Y.; Faraon, A. High efficiency double-

wavelength dielectric metasurface lenses with dichroic birefringent meta-atoms. *Opt. Express* **2016**, *24*, 18468–18477.

(48) Liu, V.; Fan, S. S4 : A free electromagnetic solver for layered periodic structures. *Comput. Phys. Commun.* **2012**, *183*, 2233–2244.

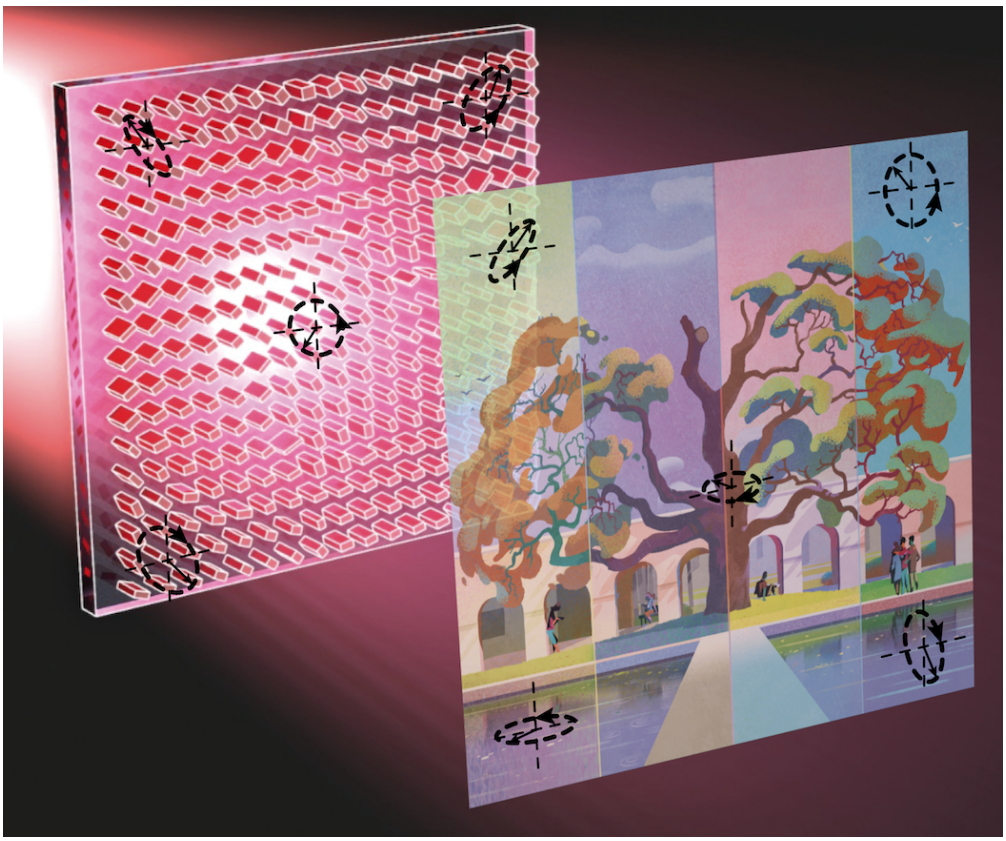

88x73mm (300 x 300 DPI)